Supplement of Atmos. Meas. Tech., 18, 3073–3093, 2025
https://doi.org/10.5194/amt-18-3073-2025-supplement

Atmospheric Measurement Techniques
Open Access
EGU

Supplement of

Characterization of filter photometer artifacts in soot and dust measurements – laboratory and ambient experiments using a traceably calibrated aerosol absorption reference

Jesús Yus-Díez et al.

Correspondence to: Jesús Yus-Díez (jesus.yus@ung.si)

Samples

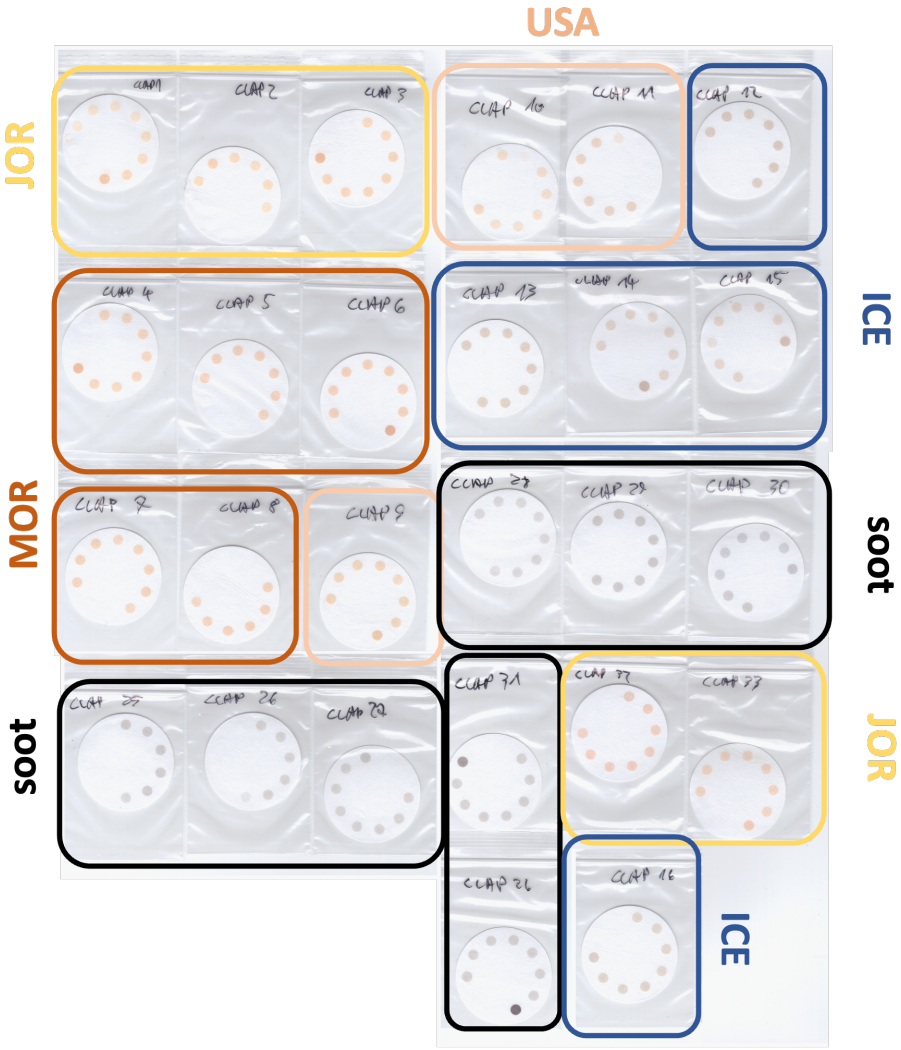

Figure S1: CLAP filter spots for all the different measured samples: JOR, MOR, USA, ICE and soot.

Uncertainty analysis for PTAAM-2λ version P02

PTAAM-2λ prototype version P01 was described in Drinovec et al. (2022). PTAAM-2λ version P02 has the same geometry of the interferometer and measurement chamber and different pump lasers: 450 and 808 nm laser diodes (instead of 532 and 1064 nm solid state lasers used in P01).

Similar to Drinovec et al. (2022) the 450 nm channel is calibrated using NO2. The calibration is transferred to 808 nm channel using polydisperse nigrosin particles and using the absorption ratio $b_{abs,808nm}/b_{abs,450nm}$ which was calculated using the Mie theory. In the uncertainty budget (Table S1) we included the uncertainty of the NO2 absorption spectrum (Vandaele et al., 2002; Orphal and Chance, 2003), which affects the uncertainties of the absorption coefficient both at 450 and 808 nm but not the uncertainty of AAE. Other sources of uncertainty are described in Drinovec et al. (2022).

Table S1: The sources of uncertainty for PTAAM-2λ PO2 measurements and combined standard uncertainties (k=1) for obtaining absorption coefficients and absorption Ångström exponent (AAE).

	Sources of uncertainty	**Uncertainty**	**Components**
A	NO_2 amount fraction	2.0%	
B	Absorption cross-section of NO_2	2.0%	
C	Mie calculation & Nigrosin refractive index	2.0%	
D	Mie calculation & Particle size distribution	4.0%	
E	Scattering & absorbing gases	1.0%	
F	Stability of instrument response	3.0%	
	Combined uncertainties		
	$b_{abs,450nm}$	4.2%	A, B, E, F
	$b_{abs,808nm}$	6.2%	A, B, C, D, E, F
	AAE	10.4%	C, D, E, F, In

Particle size distribution

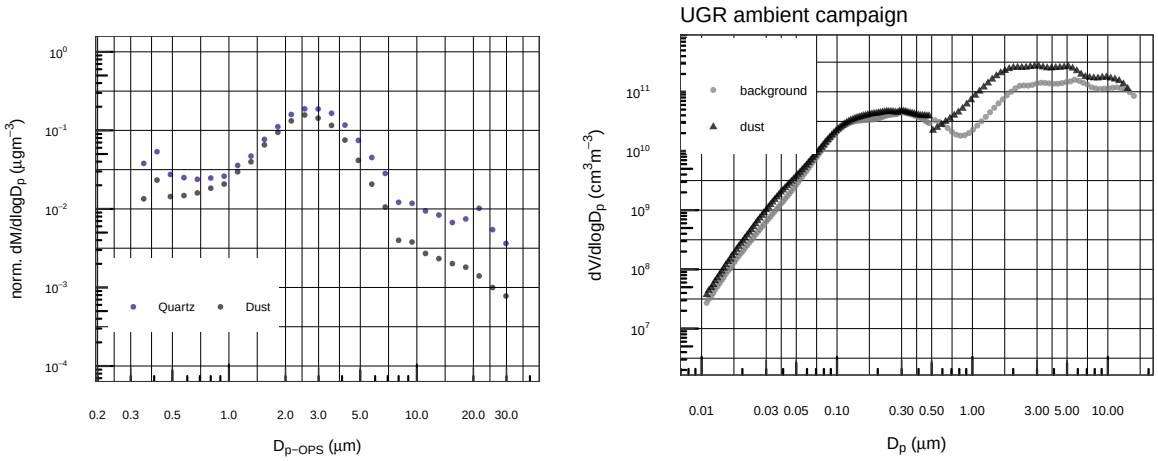

Figure S2: Left panel: Normalized mass particle size distribution for all the dust and Quartz samples resuspended in the chamber during the laboratory experiments. Right panel: Normalized volume particle size distribution during the summer 2023 AGORA campaign in Granada for both the background and Saharan dust outbreak scenarios.

FP multiple scattering

Scattering artefact

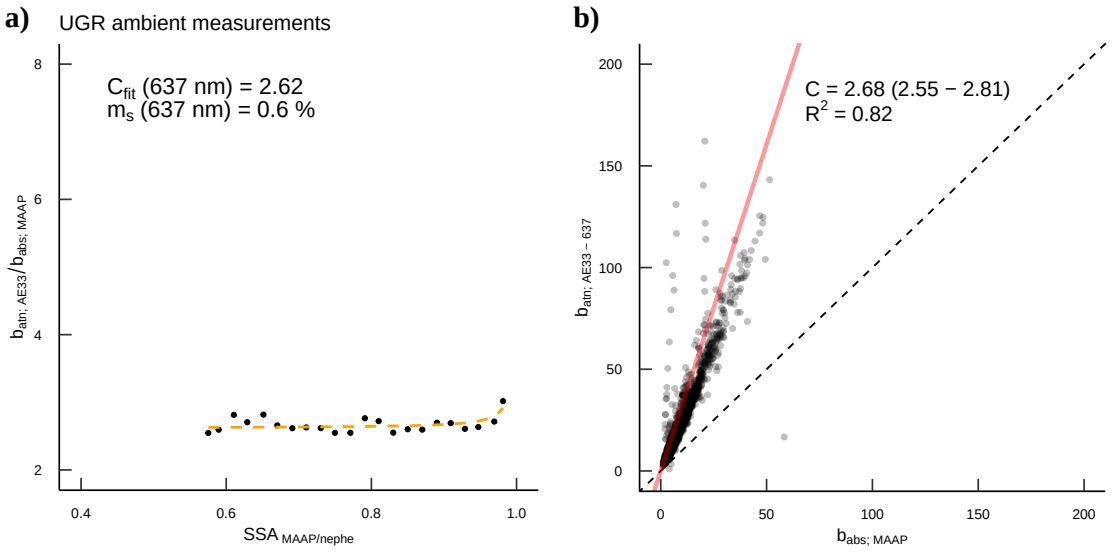

Figure S3: The filter photometer scattering artefact during the summer 2023 AGORA campaign in Granada shown as: a) the fit of the ratio of the AE33 attenuation coefficient to the MAAP absorption coefficient as a pseudo-reference measurements vs. SSA at 637 nm - parameters from fit as in Yus-Diez et al., 2021. And b), as the slope with the 95% confidence interval of the slope and the R^2 of the corrected attenuation coefficient from the AE33 using the m_s from panel (a) and the MAAP absorption coefficient as a reference absorption.

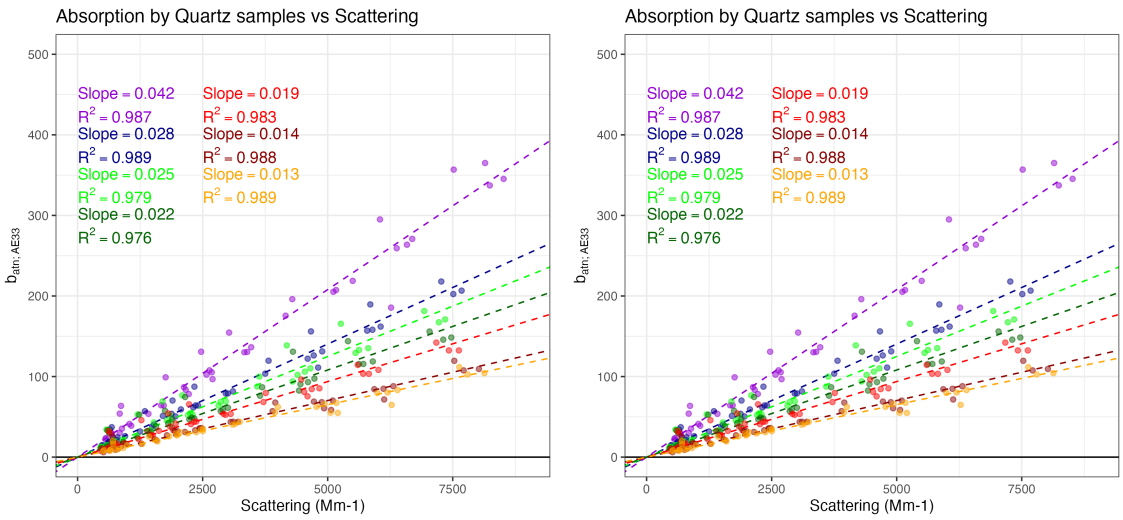

Figure S4: The filter photometer scattering artefact shown as the dependence of attenuation on the scattering coefficient in AE33 (a) and CLAP (b) during the laboratory campaign using resuspended non-absorbing Quartz samples.

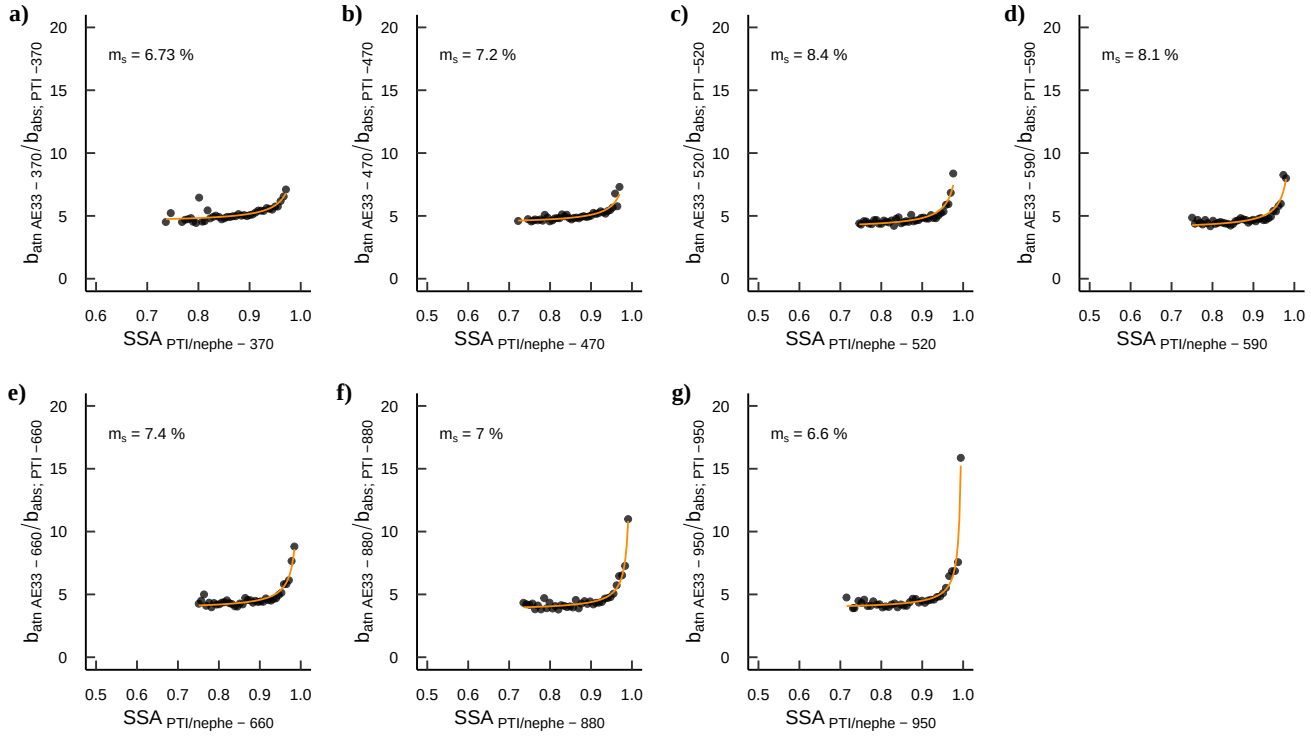

Figure S5: The filter photometer scattering artefact during the summer 2023 AGORA campaign in Granada shown as as the fit of the ratio of the AE33 attenuation coefficient to PTAAM-2λ absorption coefficient vs. SSA at AE33 wavelengths (370, 470, 520, 590, 660, 880, 950 nm) - parameters from fit as in Yus-Diez et al., 2021.

Scattering relative contribution

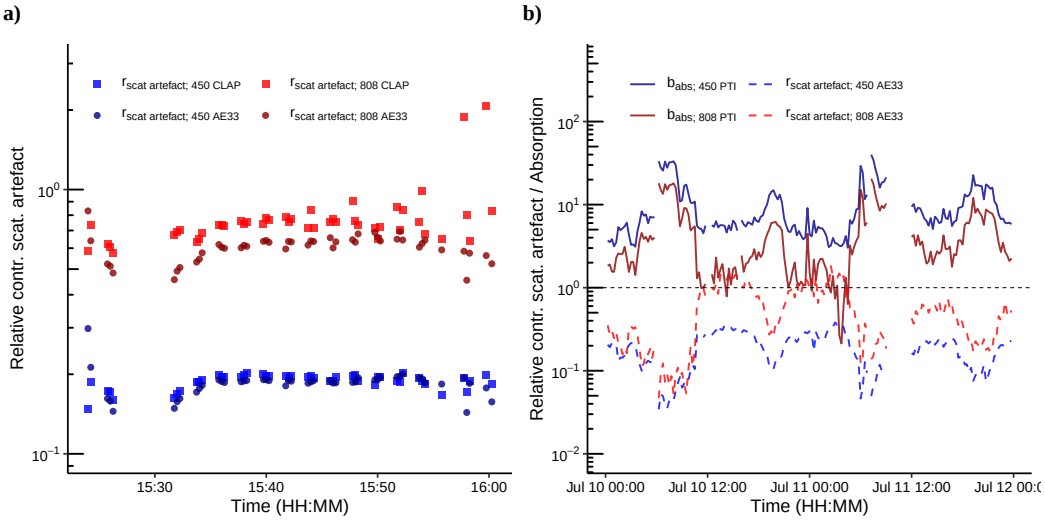

Figure S6: a) Evolution for the Morocco 31 dust sample with the wavelength of the relative contribution of the scattering artefact to the total attenuation measured by the AE33 and the CLAP (and extrapolated to the PTI wavelengths). Temporal evolution during a Saharan dust event the 10 and 11 July in Granada of the absorption coefficients measured with the PTAAM-2λ and the relative contribution of the scattering artefact to the total attenuation measured by the AE33.

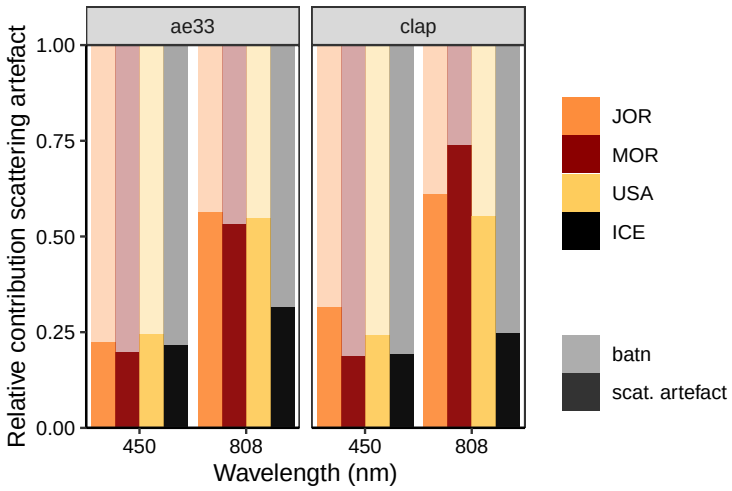

Figure S7: Relative contribution of the scattering artefact for each of the mineral samples studies at the laboratory campaign at 450 and 808 nm for the AE33 and CLAP.

Regression fits

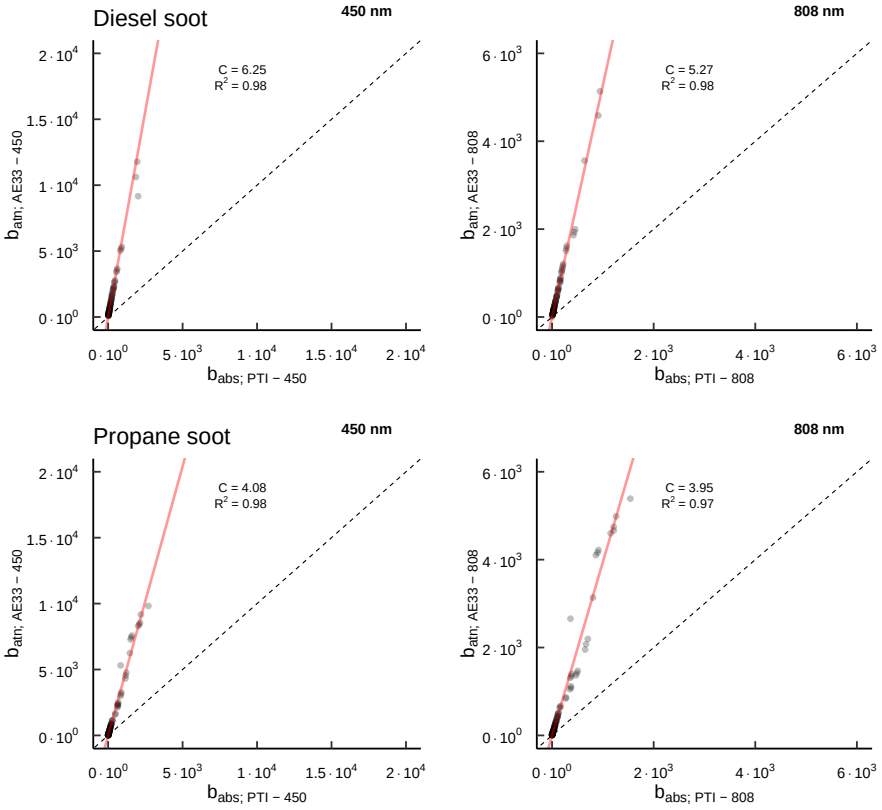

Figure S8: AE33 attenuation corrected for the scattering artefact vs the PTAAM-2λ absorption coefficient at 450 (left panels) and 808 nm (right panels) for the soot-like generated particles. In particular, each panel is for the regions: a) diesel soot as generated by an EURO 3 diesel engine, with a mean volume particle diameter of 177 nm and b) propane generated soot with a mean volume particle diameter of 341 nm. The slope represents the multiple scattering parameter C.

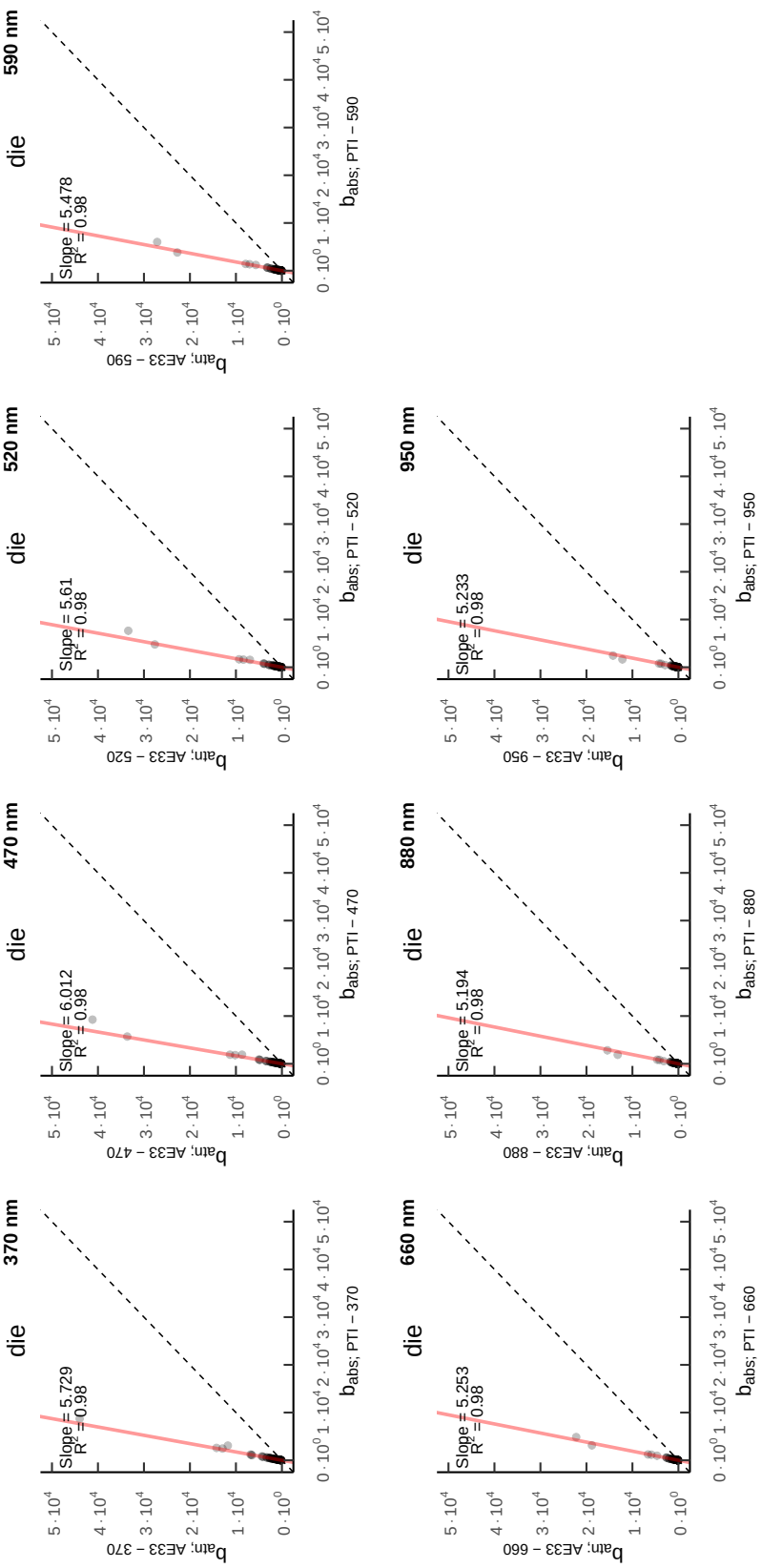

Figure S9: AE33 attenuation corrected for the scattering artefact vs the PTAAM-2λ absorption coefficient at the AE33 wavelengths: 370, 470, 520, 590, 660, 880 and 950 nm for the diesel soot particles by an EURO 3 diesel engine, with a mean volume particle diameter of 177 nm. The slope represents the multiple scattering parameter C.

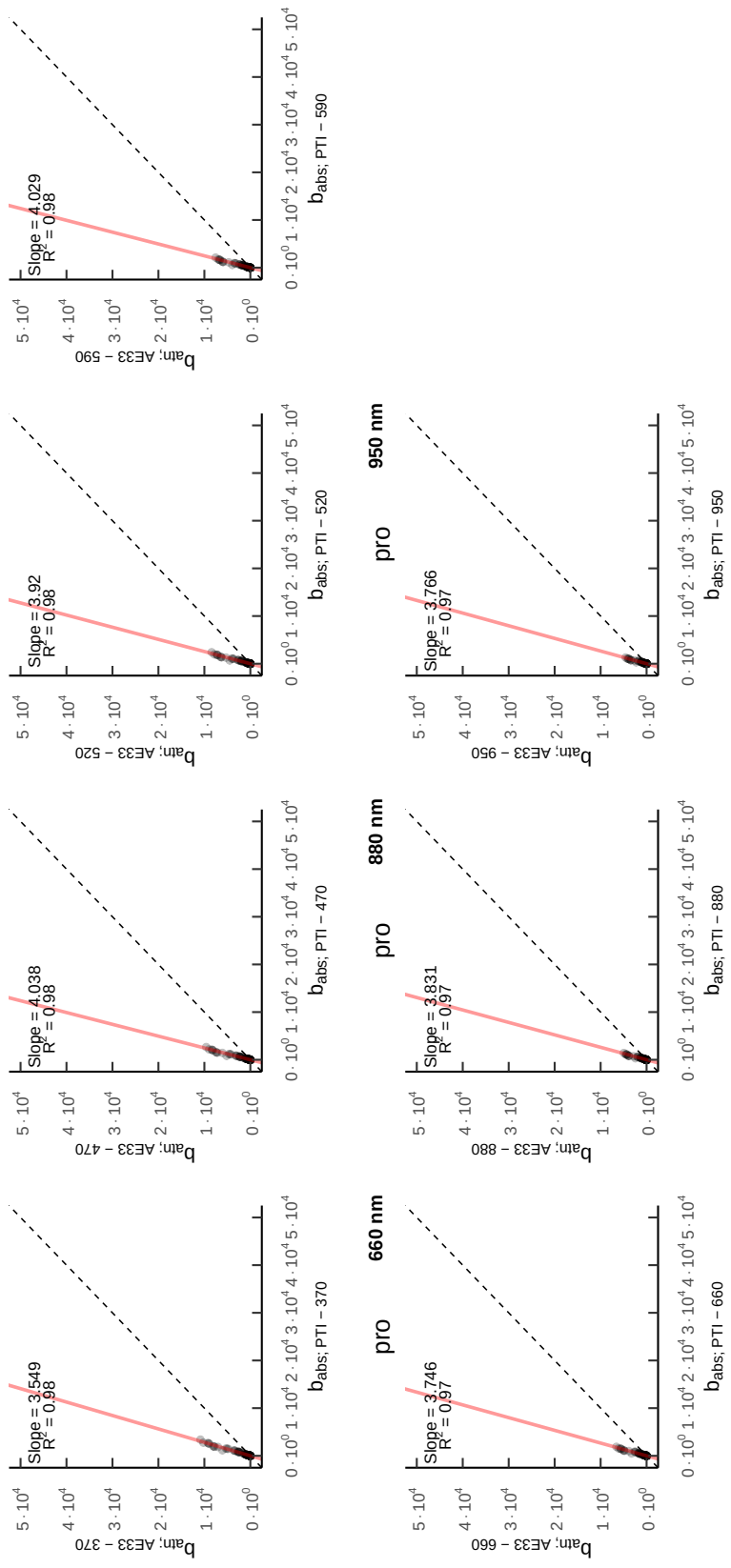

Figure S10: As Figure S9 but for propane generated soot with a mean volume particle diameter of 341 nm. The slope represents the multiple scattering parameter C.

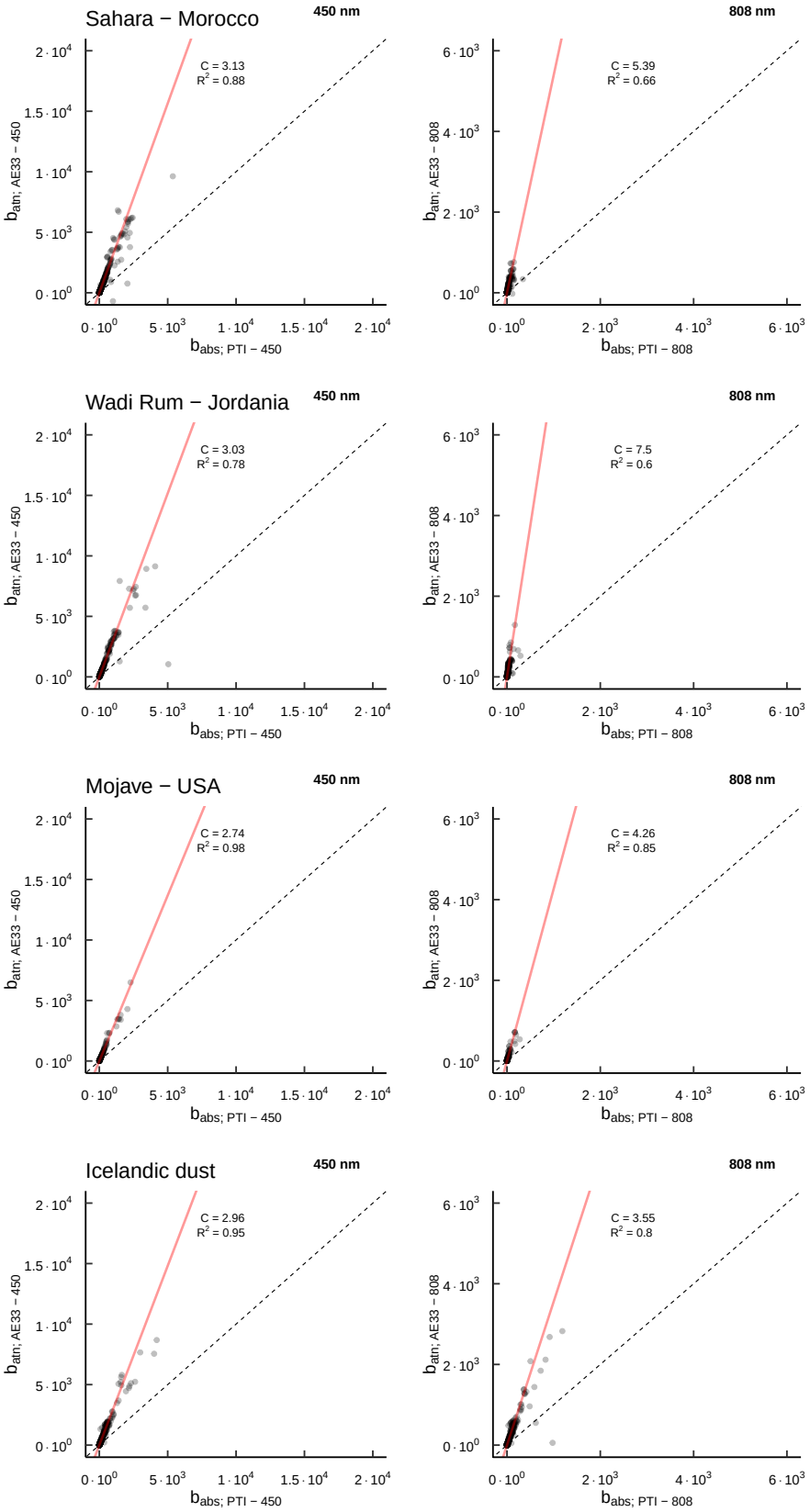

Figure S11: AE33 attenuation corrected for the scattering artefact vs the PTAAM-2λ absorption coefficient at 450 (left panels) and 808 nm (right panels) for the mineral dust samples analyzed during the laboratory experiments. In particular, each panel is for the regions: a) Saharan mineral from Morocco, b) dust from Wadi Rum, c) Mojave desert (USA) and d) Icelandic dust. The slope represents the multiple scattering parameter C.

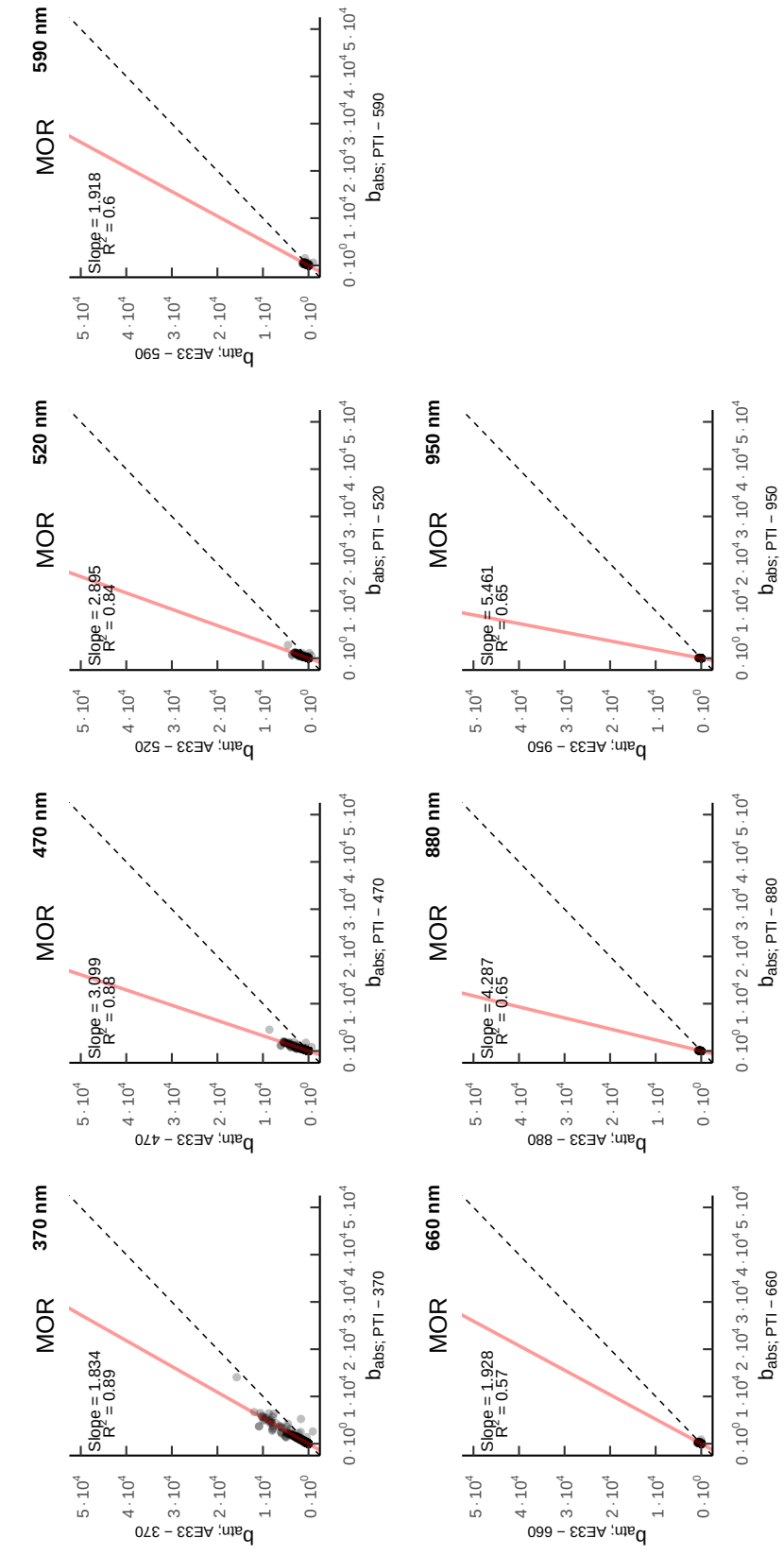

Figure S12: AE33 attenuation corrected for the scattering artefact vs the PTAAM-2λ absorption coefficient at 450 (left panels) and 808 nm at the AE33 wavelengths: 370, 470, 520, 590, 660, 880 and 950 nm for the Saharan mineral from Morocco analyzed during the laboratory experiments. The slope represents the multiple scattering parameter C.

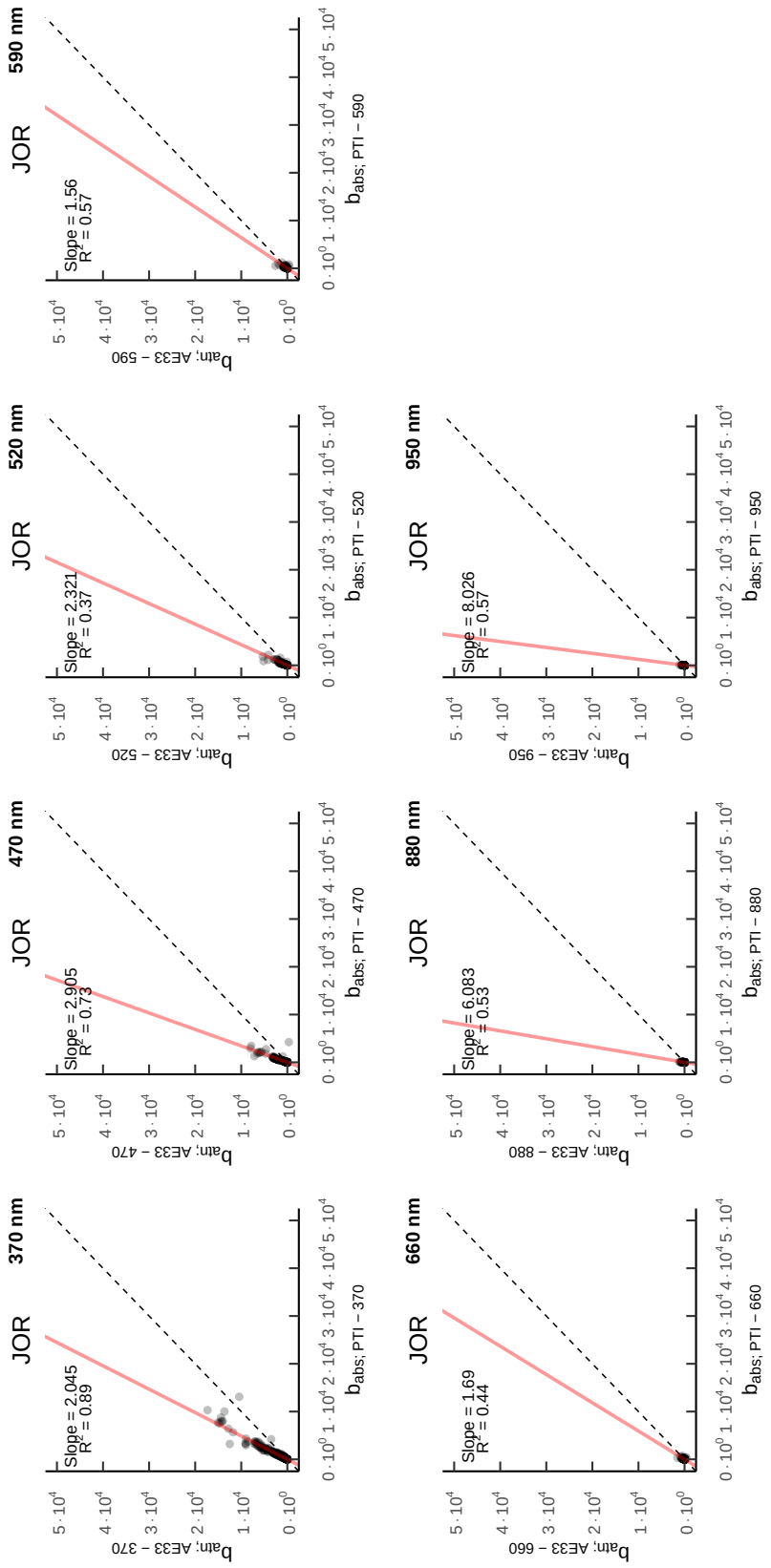

Figure S13: As Figure S12 but for dust from Jordan. The slope represents the multiple scattering parameter C.

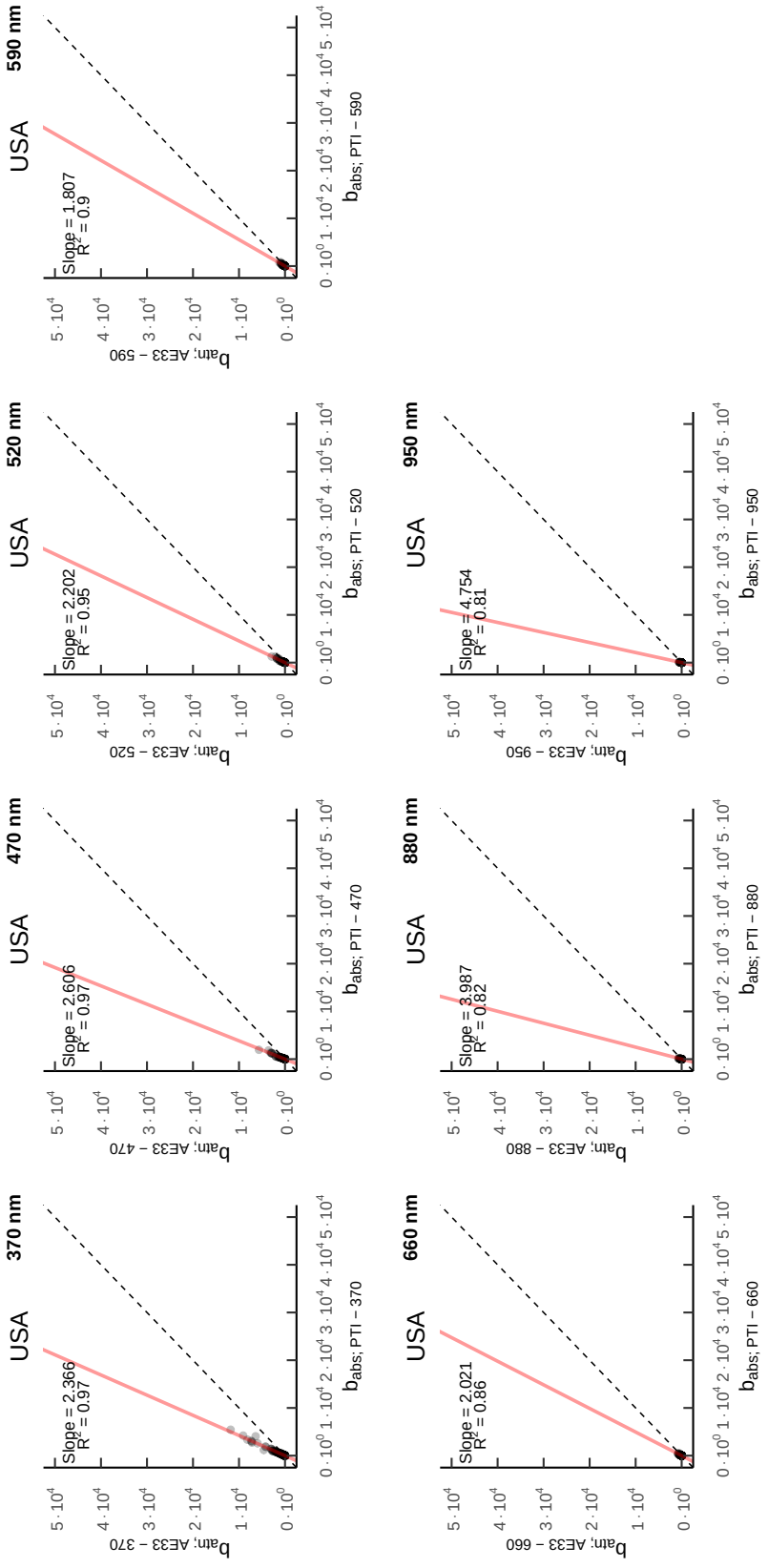

Figure S14: As Figure S12 but for dust from Mojave desert (USA). The slope represents the multiple scattering parameter C.

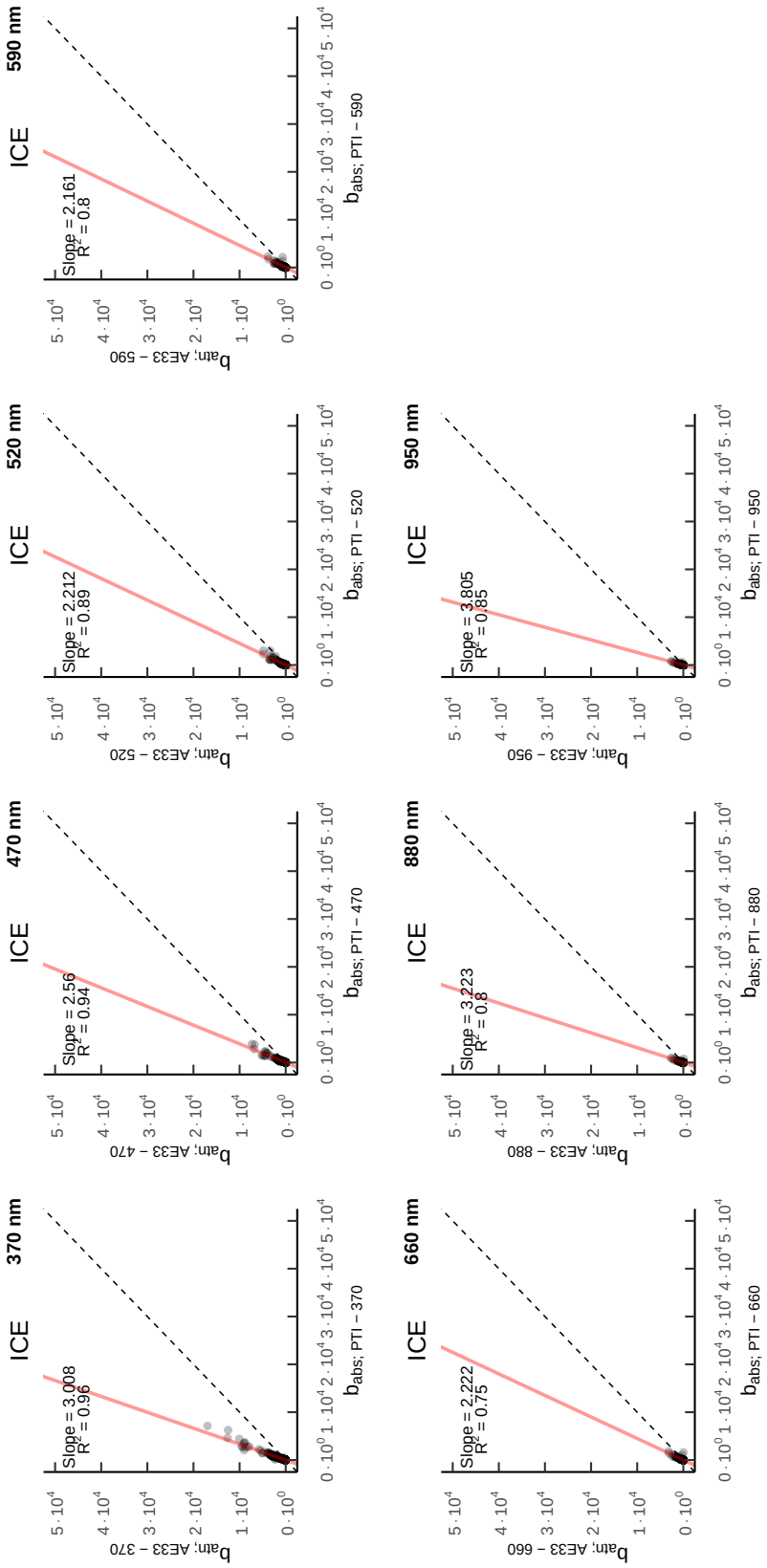

Figure S15: As Figure S12 but for Icelandic dust. The slope represents the multiple scattering parameter C.

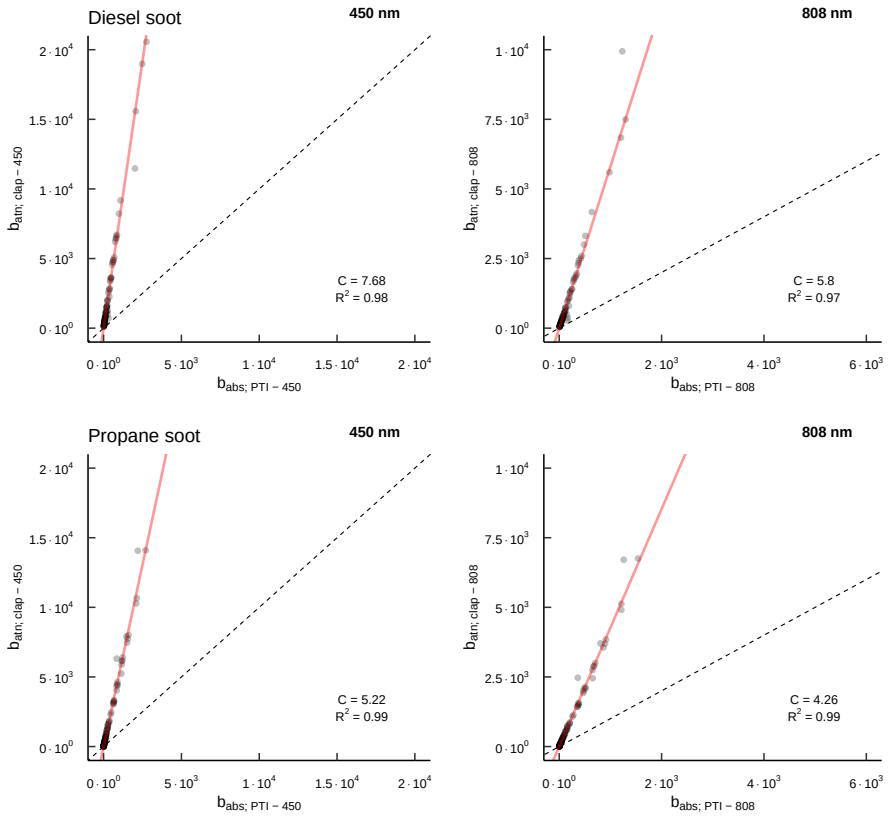

Figure S16: CLAP attenuation corrected for the scattering artefact vs the PTAAM-2λ absorption coefficient at 450 (left panels) and 808 nm (right panels) for the soot-like generated particles. In particular, each panel is for the regions: a) diesel soot as generated by an EURO 3 diesel engine, b) propane generated soot. The slope represents the multiple scattering parameter C.

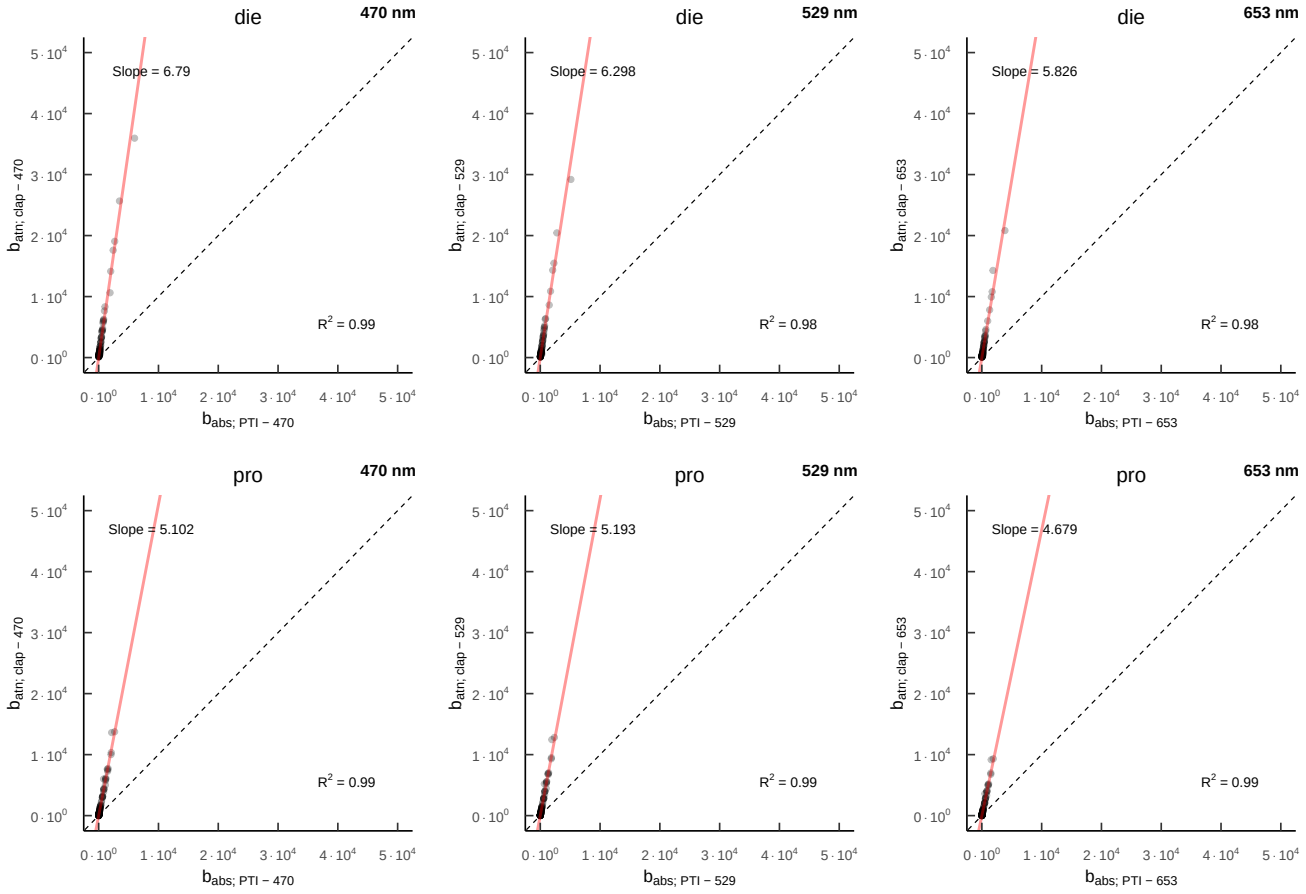

Figure S17: CLAP attenuation corrected for the scattering artefact vs the PTAAM-2λ absorption coefficient at the CLAP wavelengths (470, 529 and 653 nm) for the soot-like generated particles. In particular, each panel is for the regions: a) diesel soot as generated by an EURO 3 diesel engine, b) propane generated soot. The slope represents the multiple scattering parameter C.

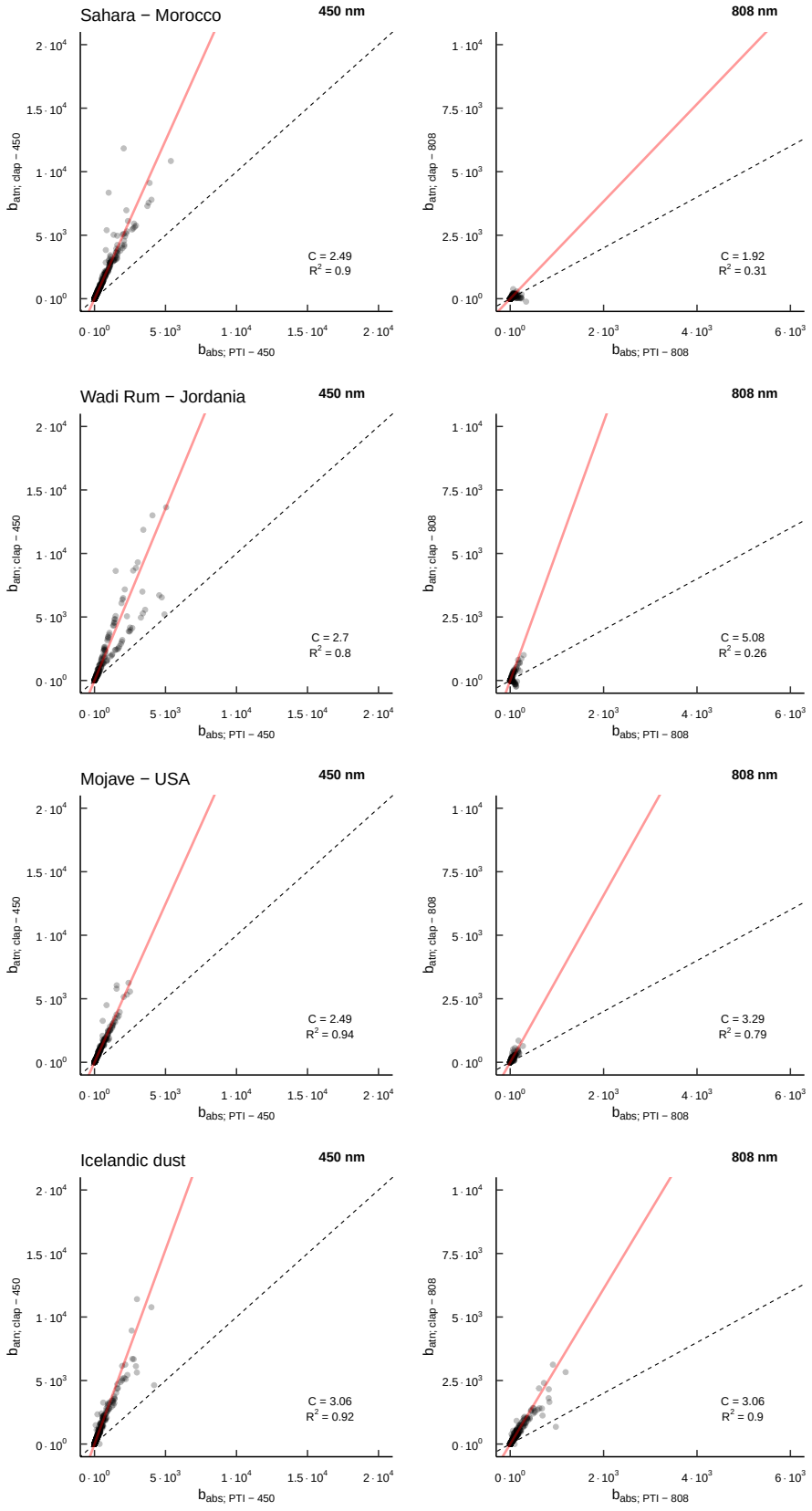

Figure S18: CLAP attenuation corrected for the scattering artefact vs the PTAAM-2λ absorption coefficient at 450 (left panels) and 808 nm (right panels) for the mineral dust samples analysed during the laboratory experiments. In particular, each panel is for the regions: a) Saharan mineral from Morocco, b) dust from Wadi Rum, c) Mojave desert (USA) and d) Icelandic dust. The slope represents the multiple scattering parameter C.

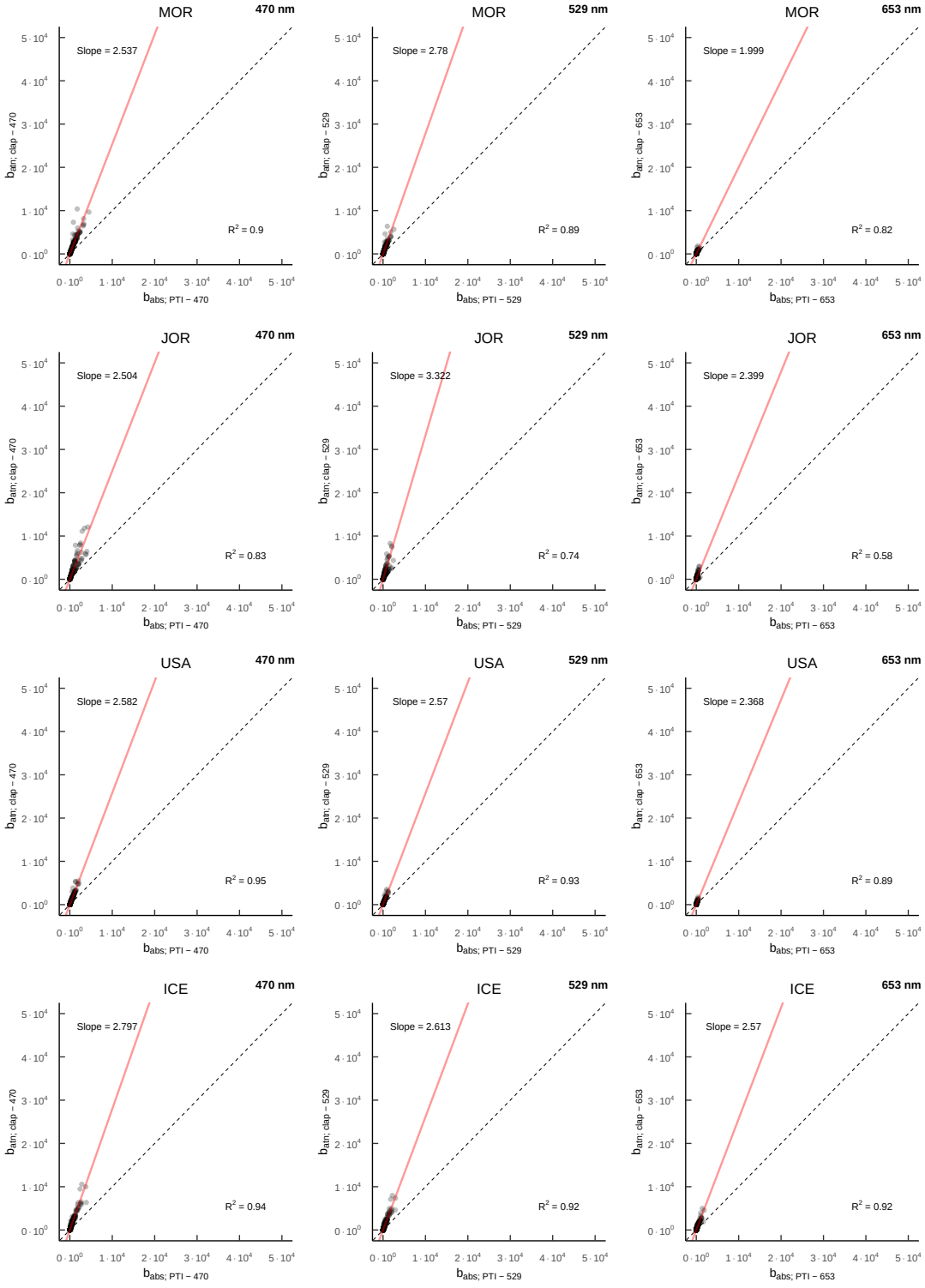

Figure S19: CLAP attenuation corrected for the scattering artefact vs the PTAAM-2λ absorption coefficient at the CLAP wavelengths (470, 529 and 653 nm) for the mineral dust samples analysed during the laboratory experiments. In particular, each panel is for the regions: a) Saharan mineral from Morocco, b) dust from Wadi Rum, c) Mojave desert (USA) and d) Icelandic dust. The slope represents the multiple scattering parameter C.

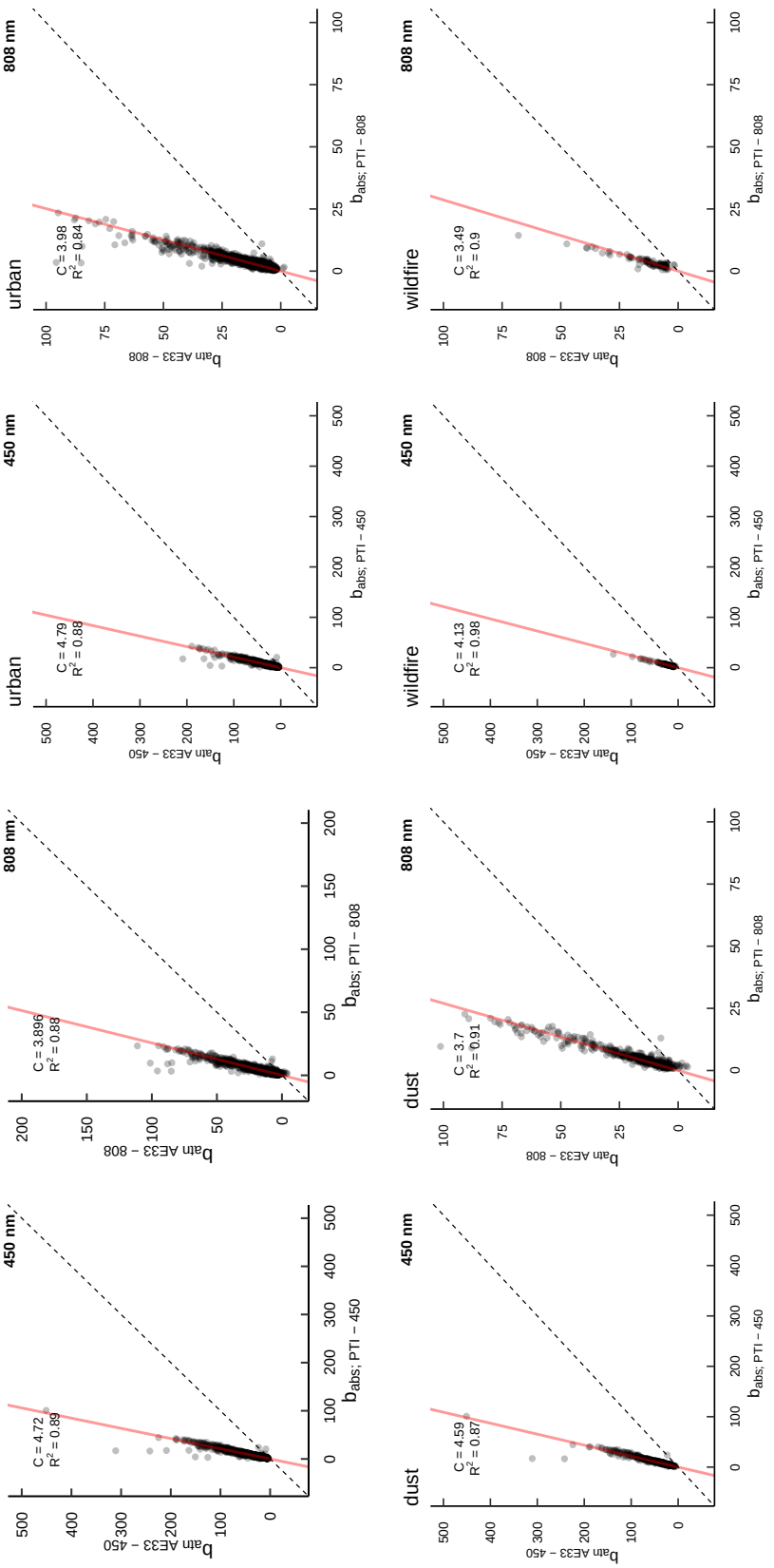

Figure S20: AE33 attenuation corrected for the scattering artefact vs the PTAAM-2λ absorption coefficient at 450 and 808 nm for the average of ambient campaign at the UGR site and the specific urban, dust + urban and wildfire + urban background preiods. The slope represents the multiple scattering parameter C.

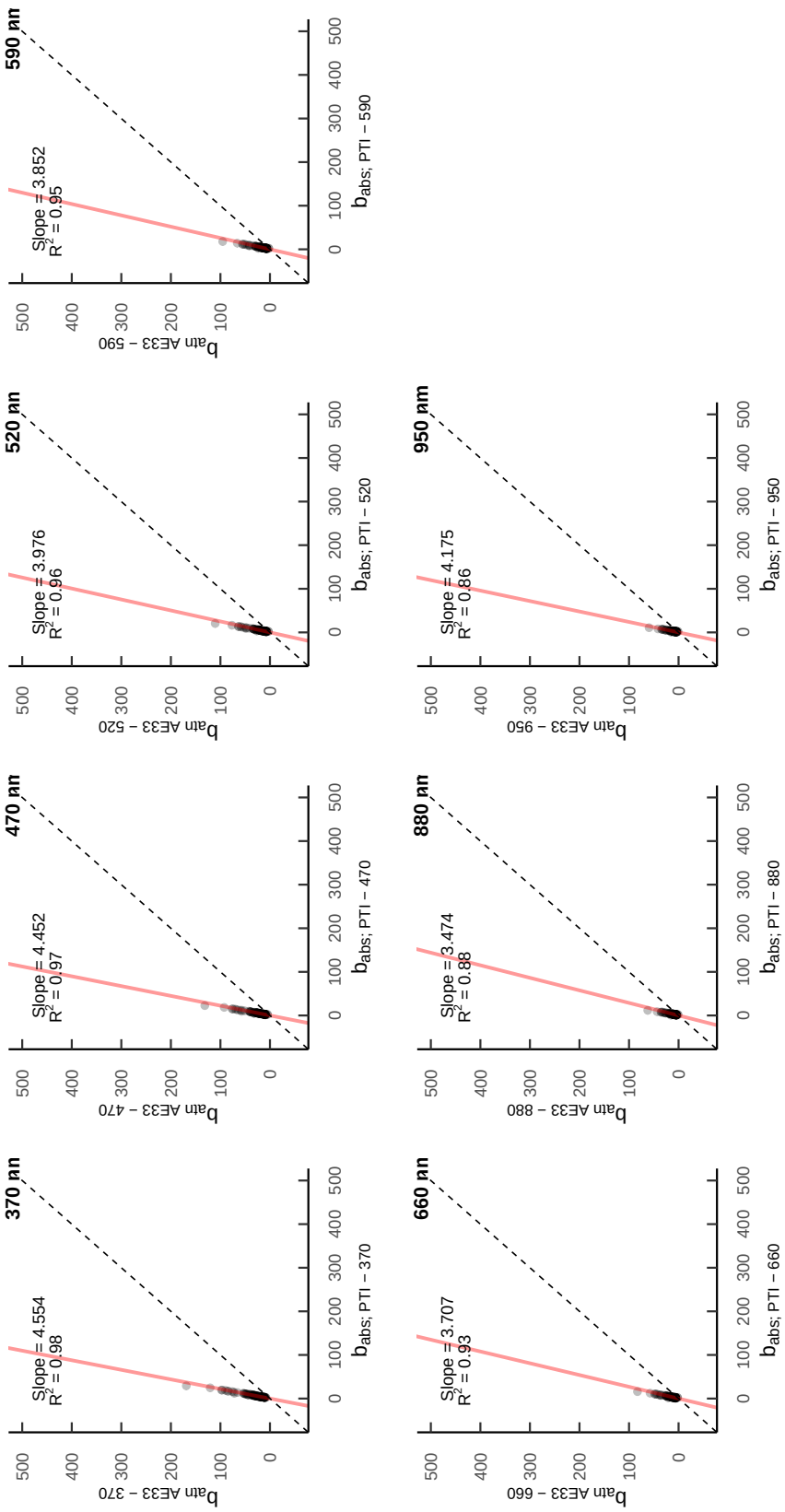

Figure S21: AE33 attenuation corrected for the scattering artefact vs the PTAAM-2λ absorption coefficient at the AE33 wavelengths 370, 470, 520, 590, 660, 880 and 950 nm for the ambient campaign at the UGR site. The slope represents the multiple scattering parameter C.

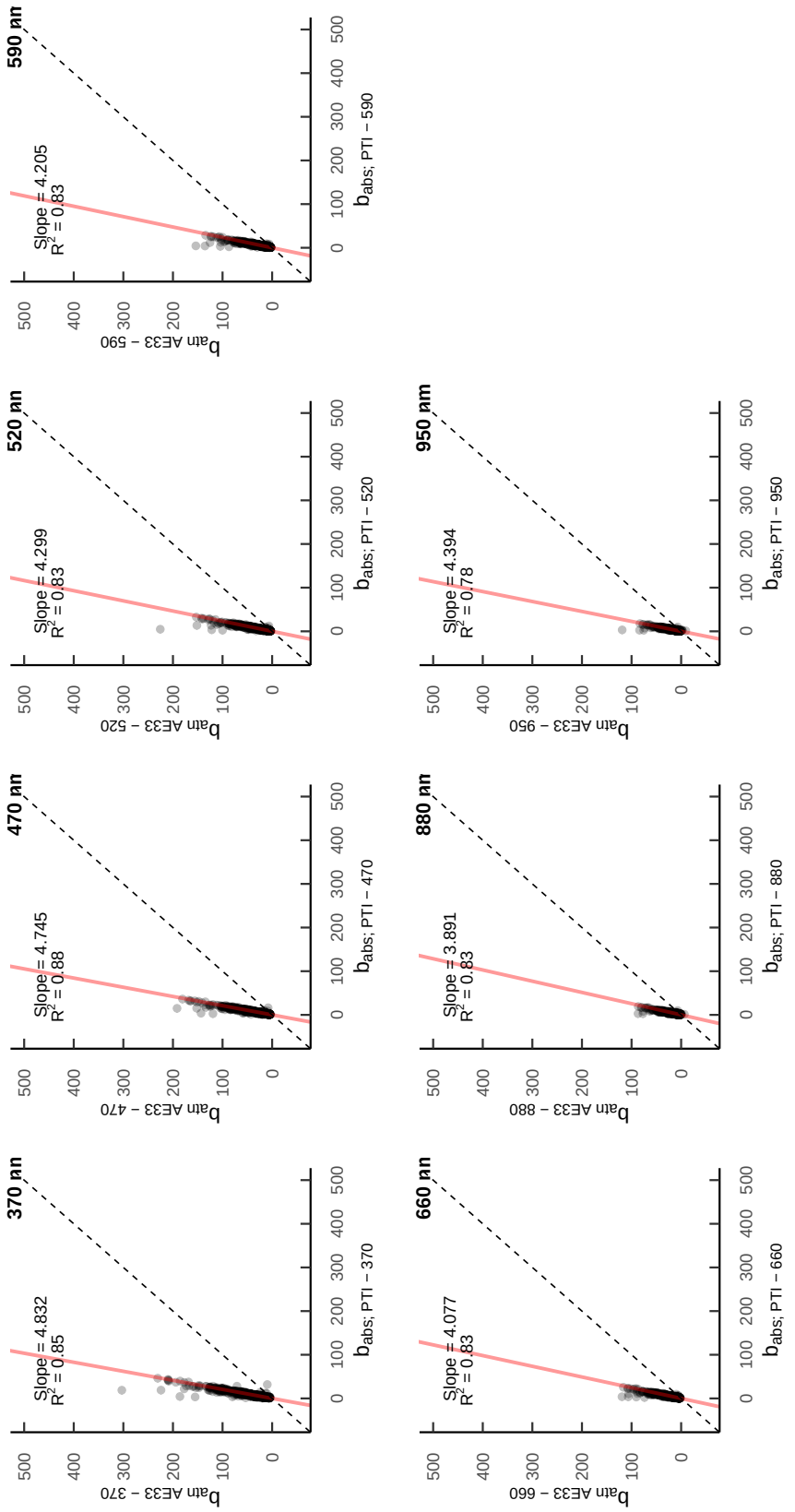

Figure S22: As Figure S21 but just for the urban background period.

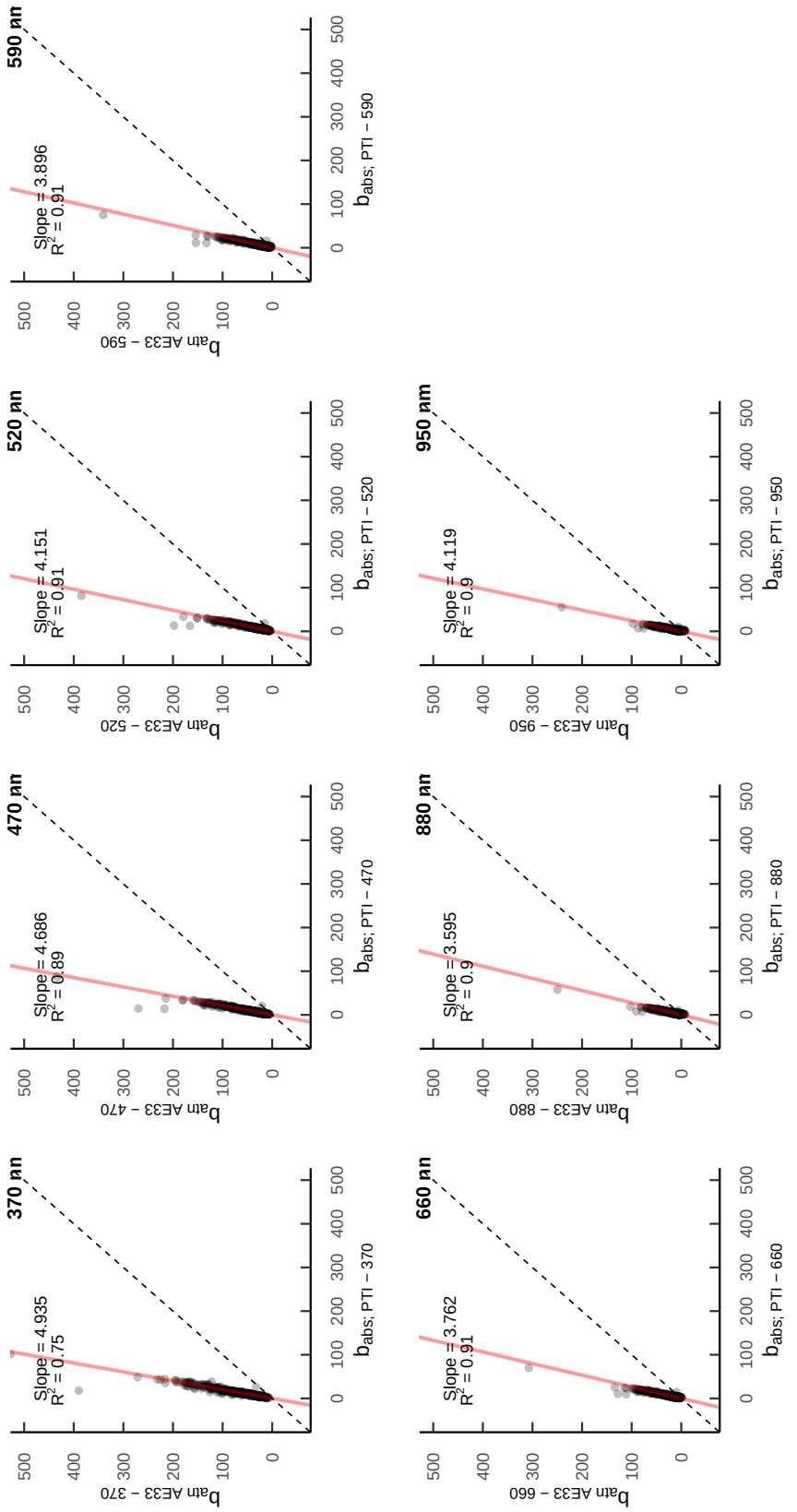

Figure S23: As Figure S21 but just for dust + urban background.

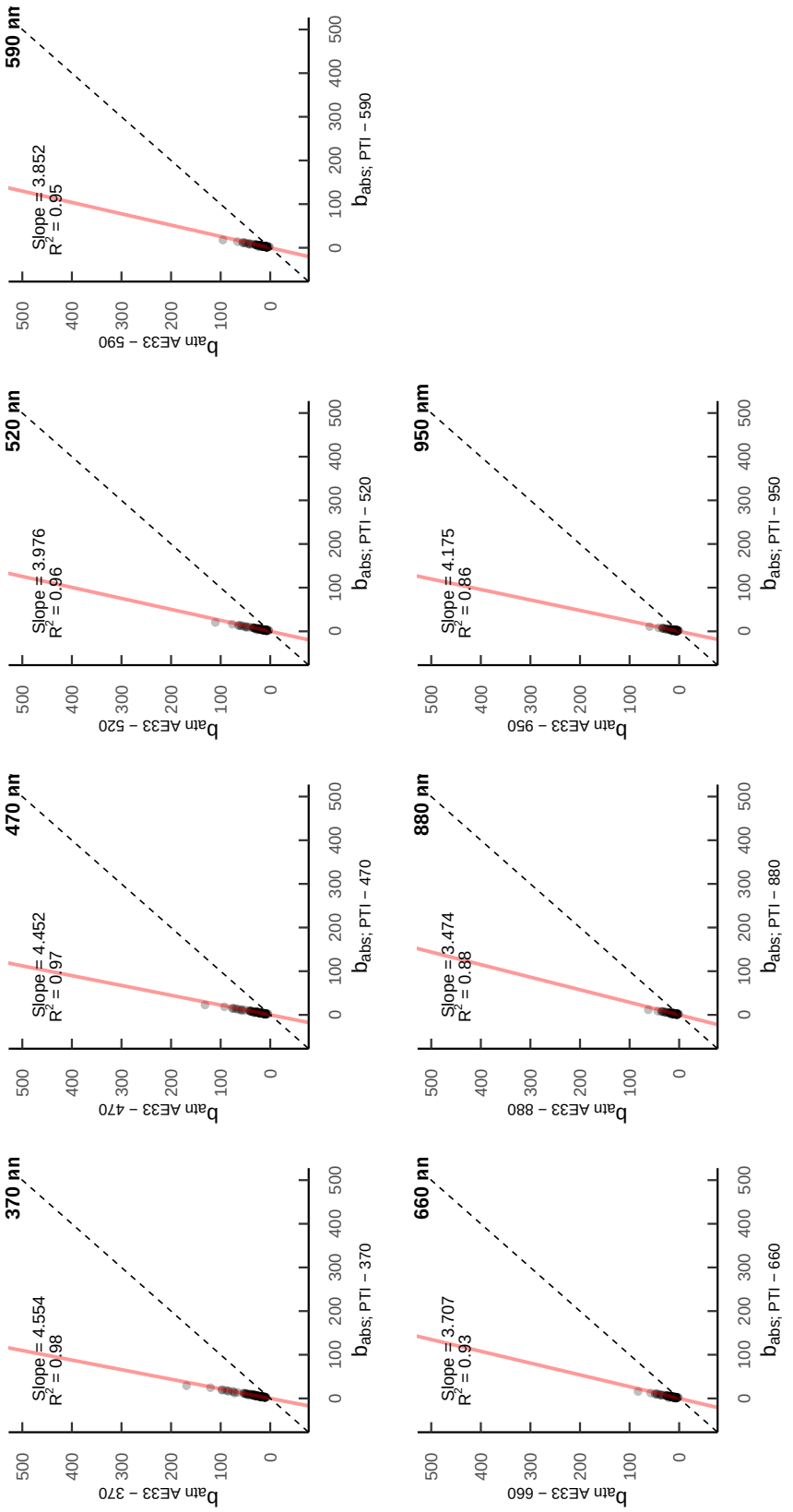

Figure S24: As Figure S21 but just for wildfire + urban background.

Table S2: Upper and a lower 95% confidence interval of the multiple-scattering parameter C for the Aethalometer AE33 (laboratory and ambient campaign) obtained as the orthogonal fit. of their attenuation coefficients corrected for cross-sensitivity to scattering vs. the PTAAM-2λ absorption coefficients (Figs. S8-S15 and S20-S24). In parenthesis, it is shown the R^2 between these two compared variables. Values have been reported at the reporting wavelengths of each FP (by inter- and extrapolation) and the wavelengths of the PTAAM-2λ at which they were measured.

	AE33: C								
Sample	**370 nm**	**450 nm**	**470 nm**	**520 nm**	**590 nm**	**660 nm**	**808 nm**	**880 nm**	**950 nm**
Icelandic dust	2.95-3.06 (0.96)	2.90-3.03(0.947)	2.51-2.61 (0.94)	2.15-2.27 (0.89)	2.10-2.22 (0.80)	2.13-2.32 (0.75)	3.39-3.72 (0.80)	3.06-3.38 (0.80)	3.67-3.94 (0.85)
Wadi Rum (Jordan)	1.99-2.10 (0.89)	2.98-3.08(0.775)	2.85-2.96 (0.72)	2.23-2.42 (0.37)	1.46-1.66 (0.57)	1.55-1.83 (0.44)	6.61-8.38 (0.60)	5.33-6.84 (0.53)	7.03-9.02 (0.57)
Sahara (Morocco)	1.79-1.88 (0.89)	3.03-3.22(0.884)	3.05-3.15 (0.88)	2.84-2.95 (0.84)	1.86-1.98 (0.60)	1.85-2.01 (0.57)	4.88-5.90 (0.66)	3.96-4.61 (0.65)	4.97-5.95 (0.65)
Mojave (USA)	2.27-2.46 (0.97)	2.66-2.81(0.976)	2.55-2.66 (0.97)	2.15-2.26 (0.95)	1.74-1.88 (0.90)	1.92-2.12 (0.86)	3.85-4.68 (0.85)	3.65-4.33 (0.82)	4.33-5.17 (0.81)
Propane Soot	3.47-3.63 (0.98)	3.98-4.18(0.982)	3.95-4.13 (0.98)	3.83-4.01 (0.98)	3.92-4.14 (0.98)	3.61-3.88 (0.97)	3.80-4.09 (0.97)	3.69-3.97 (0.97)	3.62-3.91 (0.97)
Diesel soot	5.54-5.92 (0.98)	6.08-6.43(0.980)	5.90-6.13 (0.98)	5.52-5.70 (0.98)	5.41-5.55 (0.98)	5.18-5.32 (0.98)	5.19-5.36 (0.98)	5.11-5.28 (0.98)	5.14-5.33 (0.98)
UGR - average	4.47-4.64 (0.83)	4.51-4.93 (0.88)	4.35-4.56 (0.90)	3.85-4.10 (0.87)	3.71-4.00 (0.87)	3.54-3.87 (0.87)	3.83-3.96 (0.89)	3.24-3.71 (0.86)	3.85-4.50 (0.83)
UGR - urban	4.80-4.86 (0.85)	4.52-5.06 (0.88)	4.71-4.78 (0.88)	4.26-4.33 (0.83)	4.17-4.24 (0.83)	4.04-4.12 (0.84)	3.88-4.06 (0.84)	3.84-3.94 (0.83)	4.31-4.48 (0.78)
UGR - urban + dust	4.87-5.00 (0.75)	4.35-4.84 (0.87)	4.63-4.74 (0.89)	4.09-4.21 (0.91)	3.83-3.97 (0.91)	3.69-3.83 (0.91)	3.60-3.88 (0.92)	3.51-3.68 (0.90)	3.99-4.25 (0.90)
UGR - urban + wildfires	4.47-4.64 (0.98)	4.03-4.22 (0.98)	4.35-4.56 (0.97)	3.85-4.10 (0.96)	3.71-4.00 (0.95)	3.54-3.87 (0.93)	3.33-3.67 (0.90)	3.24-3.71 (0.88)	3.85-4.50 (0.86)

Table S3: Upper and a lower 95% confidence interval of the multiple-scattering parameter C for the CLAP (laboratory campaign) obtained as the orthogonal fit of their attenuation coefficients corrected for cross-sensitivity to scattering vs. the PTAAM-2λ absorption coefficients (Figs. S16-S19).In parenthesis, it is shown the R^2 between these two compared variables. Values have been reported at the reporting wavelengths of each FP (by inter- and extrapolation) and the wavelengths of the PTAAM-2λ at which they were measured.

	CLAP: C				
Sample	**450 nm**	**470 nm**	**529 nm**	**653 nm**	**808 nm**
Icelandic dust	2.99-3.12 (0.92)	2.73-2.87 (0.94)	2.53-2.69 (0.92)	2.42-2.72 (0.92)	2.94-3.17 (0.90)
Wadi Rum (Jordan)	2.57-2.84 (0.80)	2.38-2.63 (0.83)	3.05-3.59 (0.74)	1.88-2.92 (0.58)	3.93-6.24 (0.26)
Sahara (Morocco)	2.45-2.53 (0.90)	2.51-2.57 (0.90)	2.71-2.85 (0.89)	1.88-2.12 (0.82)	1.75-2.08 (0.31)
Mojave (USA)	2.45-2.53 (0.95)	2.55-2.62 (0.95)	2.50-2.64 (0.93)	2.25-2.48 (0.90)	2.97-3.60 (0.79)
Propane Soot	5.15-5.29 (0.99)	5.03-5.17 (0.99)	5.12-5.27 (0.99)	4.61-4.75 (0.99)	4.21-4.32 (0.99)
Diesel soot	7.55-7.80 (0.99)	6.30-7.28 (0.99)	5.90-6.70 (0.98)	5.38-6.27 (0.98)	5.71-5.89 (0.97)

Table S4: CLAP parameters for the different laboratory samples as in Ogren et al. (2017) for correcting the change in attenuation by light scattering particles (K1) and the effects of filter loading and multiple-scattering enhancement effect (K2). Since K1(λ) relates directly to m_s, it has been obtained from the quartz samples for each wavelength, and applied to all the dust samples. Conversely, K2(λ), related to C, is sample dependent.

λ (nm)	K1
450	0.020
470	0.016
529	0.015
635	0.015
808	0.008

	K2				
Sample	**450**	**470**	**529**	**653**	**808**
Icelandic dust	**2.38**	2.60	2.22	2.18	**2.60**
Wadi Rum (Jordan)	**2.13**	2.30	2.82	2.04	**4.32**
Sahara (Morocco)	**2.16**	2.12	2.36	1.70	**1.63**
Mojave (USA)	**2.19**	2.12	2.18	2.01	**2.80**
Propane Soot	**4.34**	4.44	4.41	3.98	**3.62**
Diesel soot	**5.77**	6.53	5.36	4.96	**4.93**

Size dependence

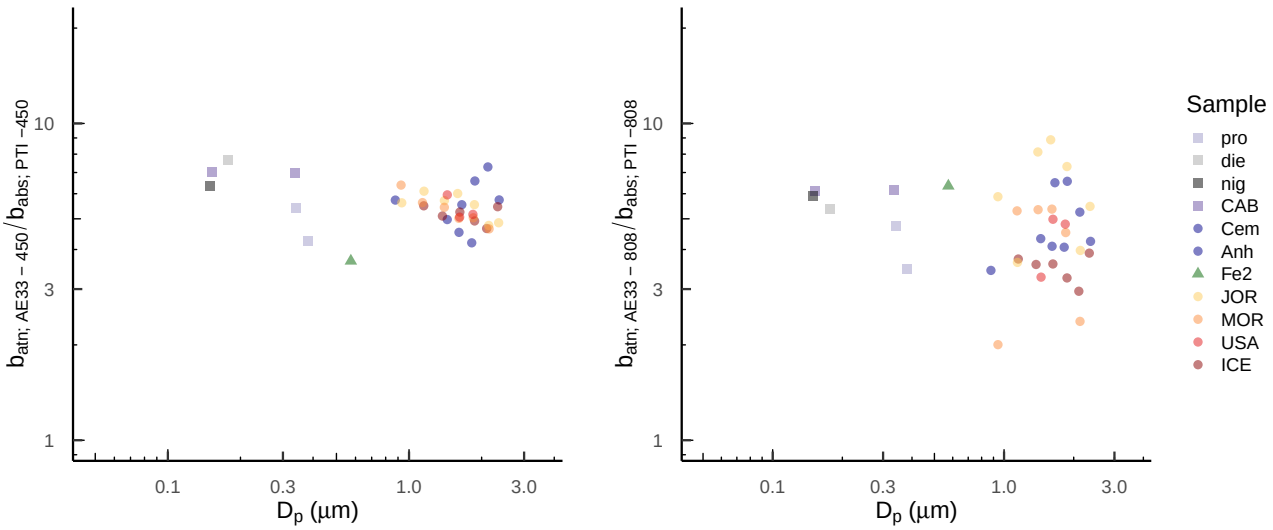

Figure S25: Multiple scattering parameter C, for AE33 and CLAP FPs vs the volume particle diameter for each of the sample groups analyzed during the laboratory measurements. It was obtained as the ratio of the FP's attenuation corrected for the scattering artefact and the PTAAM-2λ absorption coefficient at 450 and 808 nm.

MAAP absorption offset - size dependence

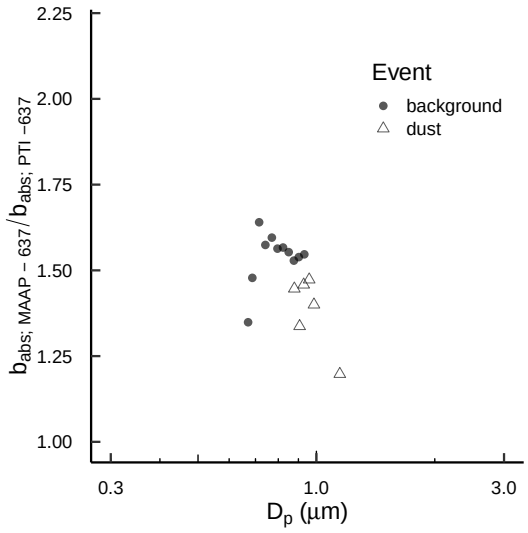

Figure S26: Evolution with size of the MAAP absorption coefficient to PTAAM-2λ absorption ratio.

Harmonization factor H^*

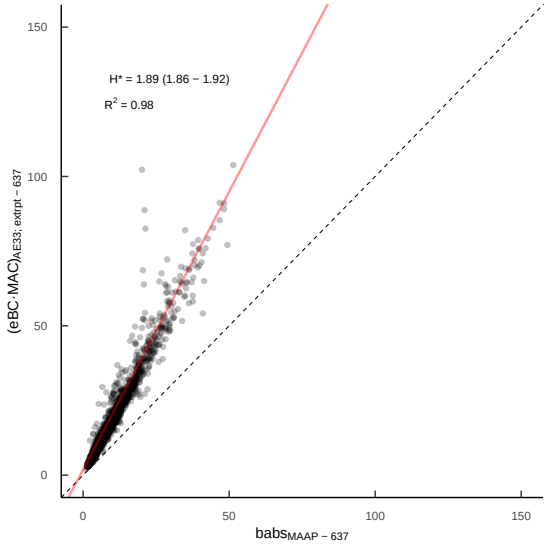

Figure S27: H^* factor computed following ACTRIS guidelines as the slope of the orthogonal fit of the AE33 eBC multiplied by its MAC (without the multiple scattering correction) and the MAAP absorption coefficients. The 95 % confidence interval is shown within the parenthesis.

References

Drinovec, L., Jagodič, U., Pirker, L., Škarabot, M., Kurtjak, M., Vidović, K., Ferrero, L., Visser, B., Röhrbein, J., Weingartner, E., Kalbermatter, D. M., Vasilatou, K., Bühlmann, T., Pascale, C., Müller, T., Wiedensohler, A., and Močnik, G.: A dual-wavelength photothermal aerosol absorption monitor: design, calibration and performance, Atmos. Meas. Tech., 15, 3805–3825, https://doi.org/10.5194/amt-15-3805-2022, 2022.

Orphal, J. and Chance, K.: Ultraviolet and visible absorption cross-sections for HITRAN, J. Quant. Spectrosc. Ra., 82, 491–504, https://doi.org/10.1016/s0022-4073(03)00173-0, 2003.

Vandaele, A. C., Hermans, C., Fally, S., Carleer, M., Colin, R., Merienne, M. F., Jenouvrier, A., and Coquart, B.: High-resolution Fourier transform measurement of the NO2 visible and nearinfrared absorption cross sections: Temperature and pressure effects, J. Geophys. Res.-Atmos., 107, ACH 3-1–ACH 3-12, https://doi.org/10.1029/2001jd000971, 2002.